GEOLOGICAL SURVEY OF CANADA
OPEN FILE 8951

Implementing a piecewise ionospheric absorption model, Ontario

T.G. Cameron

2023

Canada

**GEOLOGICAL SURVEY OF CANADA
OPEN FILE 8951**

Implementing a piecewise ionospheric absorption model, Ontario

T.G. Cameron

2023

Permanent link: https://doi.org/10.4095/331444

This publication is available for free download through GEOSCAN (https://geoscan.nrcan.gc.ca/).

Publications in this series have not been edited; they are released as submitted by the author.

Table of Contents

1 Introduction

High Frequency (HF; 3-30 MHz) radio waves can have their trajectories altered when travelling through an ionized medium. Broadly, HF radio waves are refracted away from regions of higher electron density, with more refraction occurring for lower frequencies interacting with larger electron densities. This property allows HF radio waves to propagate over large distances, up to thousands of kilometers, by refracting off the ionosphere, the ionized region of the Earth's upper atmosphere (Davies, 1990), and by reflecting off the ground. This feature makes HF radio propagation useful in many contexts, such as communications used by, for example, the aircraft industry, the Canadian Coast Guard, and the shipping industry (National Research Council, 2008; Warrington et al., 2016), as well as over-the-horizon-radar (OTHR) used by the military for long-range surveillance (e.g. Riddolls, 2006; Thayaparan et al., 2018; 2019; 2020). HF radio wave propagation is especially important in locations such as northern Canada, where the infrastructure for alternative communication and surveillance technologies does not exist.

The ionosphere is comprised of several distinct layers, which are distinguished by their electron density profile, altitude and source of ionization. HF radio wave refraction typically occurs in the F region (150-800 km altitude) of the ionosphere, while radio wave absorption typically occurs in the lower altitude D region (50-90 km). The E region (90-150 km) is located between the F and D regions, and is known to both refract and absorb HF radio waves. E-region absorption typically occurs in the lower parts of the E-region, and has been shown with models to be comparable to D region absorption in some cases (e.g. George and Bradley, 1973; Pederick and Cervera, 2014, Zawdie et al., 2017). High amounts of absorption along a propagation path can considerably reduce received signal power, or even prevent a signal from being received entirely. Absorption occurs when radio wave energy is dissipated as heat through collisions between ionospheric particles (Davies, 1990). It is dependent on the electron density and electron collision frequency along the propagation path, and affects lower frequency waves more than higher frequency waves. Absorption occurs largely in the D and E regions because the neutral density and subsequent electron collision frequency is too low in the F region for appreciable absorption to occur.

In the absence of space weather effects, ionospheric absorption is primarily dependent on solar ionization, and varies predictably over the course of the day. This diurnal D region ionization and subsequent absorption tends to be highest at local noon, when the Sun is at its highest point in the sky. As the Sun sets, D region ionization and absorption decreases, reaching a minimum around local midnight. Many different empirical D region absorption models have been produced over the years (e.g. Lucas and Haydon, 1966; George and Bradley, 1974). These models parameterize diurnal D-region absorption with quantities such as solar zenith angle, electron cyclotron frequency, and sunspot number using empirical absorption measurements.

Some space weather phenomena such as solar flares and solar energetic particle precipitation can temporarily increase the electron density in the low-altitude ionosphere (the D and E regions), leading to increased absorption beyond what is expected from diurnal solar radiation. For example, solar flares expose the dayside of the Earth to high-energy x-ray radiation causing enhanced photoionization, and subsequently increased ionospheric absorption for periods of several minutes to a few hours (e.g. Davies, 1990; Mitra, 1974). Empirical models of space weather related absorption, such as the D Region Absorption Prediction model (D-RAP, http://www.swpc.noaa.gov/products/d-region-absorption-predictions-d-rap), which models absorption associated with solar X-ray flares and solar energetic proton events, can inform radio operators when impacts are likely. D-RAP reports the attenuation

expected for a 30 MHz radio wave passing vertically through the D region in excess of the expected diurnal variation.

Absorption models can be used to improve predictions of received signal power provided by raytracing simulations of HF radio propagation. Raytracing is a technique in which radio waves are idealized as a set of one-dimensional "rays". The trajectories of these rays are then predicted by calculating the index of refraction in a model of the ionosphere, and then solving for the trajectory by numerically integrating the Hamiltonian ray path equations (Haselgrove, 1963). Raytracing simulations of HF radio propagation can be a useful tool in support of HF radio technologies. For example, OTHR operators often use raytracing simulations to determine which frequencies will reach a surveillance target location with the highest possible signal power (e.g. Thayaparan et al., 2020, 2019). These simulations require accurate computation of absorption experienced by a radio wave for their results to be accurate.

A computationally inexpensive way to compute absorption for a given ray path is to utilize the previously mentioned D region crossing models of absorption. However, these models assume only non-deviative absorption occurs, which is true for ray paths that pass in a straight line through D region. They do not consider absorption that occurs near the reflection point. Additionally, these models often provide absorption at a single frequency that needs to be converted to absorption at the correct frequency. Non-deviative absorption is known to be inversely proportional to the square of frequency (Davies, 1990). However, this relationship is more complicated for more realistic, partially deviative propagation paths (Fiori et al., 2022; Sauer and Wilkinson, 2008; Schumer, 2010), especially at low frequencies where reflection tends to happen closer to the D region.

A more accurate, albeit computationally intensive method is to integrate absorption along the ray path, utilizing the index of refraction. In brief, models of electron and neutral density, temperature, and magnetic field are used to compute the index of refraction with the Appleton-Hartree equation, a foundational radio physics equation which describes the refractive index for an electromagnetic wave propagating through a cold, magnetized plasma. The imaginary part of the index of refraction is then used to integrate absorption along the ray path. This method accurately reflects sources of ionospheric absorption accounted for by the models used to compute the refractive index. However, this also means that sources of absorption not accounted for in the input models will not be reflected in the final absorption computation.

In this document, the implementation of an ionospheric absorption model intended for use at high latitudes applied to an existing ionospheric raytracer is described in detail. This model is based on the semi-empirical absorption model described in Pederick et al. (2014), with modification following observations by Zawdie et al. (2017). This model will be referred to as the Appleton-Hartree absorption model, or A-H model going forward. First, the theory behind computing ionospheric absorption used in the model is detailed, including methods for computing electron-ion and electron-neutral collision frequencies. Then, the implementation of this absorption model is described in detail, as well as the ionospheric raytracer and necessary ionospheric models. This model is demonstrated with an example raytrace run. Finally, some considerations and caveats for using the model are detailed.

2   Theory

2.1   Absorption Calculation

Absorption experienced by a radio wave along a propagation path (in dB) is

$$L = 8.68 \int \frac{2\pi f \operatorname{Im}(n)}{c} ds \qquad (1)$$

where ds is the distance along the wavepath, $\operatorname{Im}(n)$ is the imaginary part of the complex index of refraction (n), f is the wave frequency in Hz, and c is the speed of light in a vacuum (Davies, 1990). The factor of 8.86 converts absorption from units of nepers to dB.

For propagation in a cold plasma, the index of refraction (n) can be arrived at by using the Appleton-Hartree equation (Davies, 1990), which can be written as (e.g., Davies, 1990):

$$n^2 = 1 - \frac{2X(1 - iZ - X)}{2(1 - iZ)(1 - iZ - X) - Y^2 \sin^2 \theta \pm \sqrt{Y^4 \sin^4 \theta + 4Y^2 \cos^2 \theta \, (1 - iZ - X)^2}}. \qquad (2)$$

In Equation 2, θ is the angle between the magnetic field and the propagation direction. The $\pm$ in the denominator selects the propagation mode. The $+$ sign indicates ordinary (O) mode propagation, while the $-$ sign indicates extraordinary (X) mode propagation. X, Y, and Z are ratios comparing the plasma frequency (f_N), the electron cyclotron frequency (f_B), and the electron collision frequency (v_e) respectively to the radio wave frequency (f). These are defined as

$$X = \frac{f_N}{f}, \qquad (3)$$

$$Y = \frac{f_B}{f}, \text{ and} \qquad (4)$$

$$Z = \frac{v_e}{2\pi f}, \qquad (5)$$

respectively. For reference, plasma frequency is

$$f_N = \frac{1}{2\pi} \sqrt{\frac{n_e e^2}{\epsilon_0 m_e}}, \qquad (6)$$

and the electron gyrofrequency is

$$f_B = \frac{Be}{2\pi m_e}, \qquad (7)$$

where n_e is the electron density, e is the elementary charge, m_e is the electron mass, ϵ_0 is the permittivity of free space, and B is the magnitude of the magnetic field.

The electron collision frequency in Equation (5) is more complicated to calculate than the plasma frequency and electron cyclotron frequency. This is because collision frequency depends on the sum of contributions from different particle species, which each have distinct collisional cross sections that need to be accounted for. Some of these contributions have analytic expressions that can be derived from

3

theory, while others can only be expressed approximately using data from experiments. Additionally, assumptions made in deriving the Appleton-Hartree equation affect the kind of collision frequency required. Zawdie et al. (2017) investigated how different equations for the refractive index and different formulations of collision frequency affect absorption calculations. They noted that the Appleton-Hartree equation was derived under the assumption that the electron collision frequency does not vary with electron energy. Therefore, the Appleton-Hartree equation yields a refractive index able to accurately reflect absorption in all regions of the ionosphere only if an effective electron collision frequency, averaged over the electron velocity distribution is used. The following subsection describes the calculation of an effective electron collision frequency for use in calculating absorption with the Appleton-Hartree equation.

2.2 Effective Electron Collision Frequency

The effective electron collision frequency can be separated into two terms; the electron-ion collision frequency (ν_{ei}), and the electron-neutral collision frequency (ν_{en}).

$$\nu_e = \nu_{\text{en}} + \nu_{\text{ei}} \tag{8}$$

The electron-neutral collision frequency (ν_{en}) measures how often collisions occur between electrons and any neutral particle species. Electron-neutral collisions dominate at altitudes < 150 km, and are responsible for the vast majority of absorption that occurs in the D and E regions. The effective electron-neutral collision frequency cannot be derived from theory alone. Instead, empirical formulas have been created using real-world measurements of collisional cross sections for different neutral particle species. Schunk and Nagy (2009) assembled formulas for effective electron-neutral collision frequencies for the highest contributing atmospheric neutral particle species, which can be summed to get a total effective electron-neutral frequency. In total,

$$\nu_{\text{en}} = \nu_{eN_2} + \nu_{eO_2} + \nu_{eO} + \nu_{eHe} + \nu_{eH}, \tag{9}$$

where the individual collision frequency contributions are

$$\nu_{eN_2} = 2.33 \times 10^{-11} \, n_{N_2}(1 - 1.21 \times 10^{-4} \, T_e)T_e, \tag{10}$$

$$\nu_{eO_2} = 1.82 \times 10^{-10} \, n_{O_2}\left(1 + 3.6 \times 10^{-2}T_e^{\frac{1}{2}}\right)T_e^{\frac{1}{2}}, \tag{11}$$

$$\nu_{eO} = 8.9 \times 10^{-11} \, n_O(1 + 5.7 \times 10^{-4}T_e)T_e^{\frac{1}{2}}, \tag{12}$$

$$\nu_{eHe} = 4.6 \times 10^{-10} \, n_{He}T_e^{\frac{1}{2}}, \text{and} \tag{13}$$

$$\nu_{eH} = 4.5 \times 10^{-9} \, n_H(1 - 1.35 \times 10^{-4} \, T_e)T_e^{\frac{1}{2}}, \tag{14}$$

where T_e is the electron temperature, and n is the number density of different particle species. For example, n_{He} is the number density of Helium (He). Zawdie et al. (2017) noted that while atomic Argon

makes up a significant fraction of the atmosphere, its contribution to the electron- neutral collision frequency is ~1% (Aggarwal et al., 1979) and therefore it can be safely neglected.

The electron-ion collision frequency is a measure of how often collisions occur between electrons and ions. These collisions dominate at altitudes > ~150 km compared to electron-neutral collisions, and can cause small amounts of absorption in the F region of the ionosphere (Zawdie et al., 2017). Electron-ion collisions are well understood; Schunk and Nagy (1978) calculated the electron-ion collision frequency as (in Gaussian units):

$$\nu_{ei} = \frac{4\sqrt{2\pi}}{3} \frac{(z_i e^2)^2}{\sqrt{m_e}} \frac{n_i \ln \Lambda}{(k_B T_e)^{\frac{3}{2}}} \tag{15}$$

where z_i is the ion charge number, N_i is the ion density, and k_B is the Boltzmann constant. The Coulomb logarithm ($\ln \Lambda$) is defined as

$$\ln \Lambda = \ln \left(\frac{4k_B}{\gamma^2 z_i e^2} \frac{T_e}{k_e} \right) - \frac{(k_e^2 + k_i^2)^{\frac{1}{2}}}{k_i^2} \ln \left(\frac{(k_e^2 + k_i^2)^{\frac{1}{2}}}{k_e} \right). \tag{16}$$

The terms k_i^2 and k_e^2 are,

$$k_i^2 = \frac{4\pi z_i^2 e^2 n_i}{k_B T_i}, \tag{17}$$

$$k_e^2 = \frac{4\pi e^2 n_e}{k_B T_e}, \tag{18}$$

respectively, where γ is the Euler-Mascheroni constant, and T_i is the ion temperature.

For implementation in code, the equations describing electron-ion collision frequency were converted to SI units, and constant factors were pre-calculated. The vast majority of ions were assumed to be singly ionized, setting $z_i = 1$. Additionally, the ionosphere was assumed to be neutral, so that $n_e = n_i$. This allowed the local electron density to be substituted in for the ion density. These equations are shown below:

$$\begin{aligned} \nu_{ei} &= \frac{4\sqrt{2\pi}}{3} \left(\frac{1}{4\pi\epsilon_0} \right)^2 \frac{e^4}{\sqrt{m_e}} \frac{n_i \ln \Lambda}{(k_B T_e)^{\frac{3}{2}}} \\ &= 3.63315257 \times 10^{-6} \text{m}^3 \text{K}^{3/2} \text{s}^{-1} \frac{n_i \ln \Lambda}{T_e^{\frac{3}{2}}} \end{aligned} \tag{19}$$

$$\ln \Lambda = \ln \left(\frac{4k_B (4\pi\epsilon_0)}{\gamma^2 e^2} \frac{T_e}{k_e} \right) - \frac{(k_e^2 + k_i^2)^{\frac{1}{2}}}{k_i^2} \ln \left(\frac{(k_e^2 + k_i^2)^{\frac{1}{2}}}{k_e} \right)$$

$$= \ln\left(718463.754 \text{ m}^{-1}\text{K}^{-1}\frac{T_e}{k_e}\right) - \frac{(k_e^2 + k_i^2)^{\frac{1}{2}}}{k_i^2}\ln\left(\frac{(k_e^2 + k_i^2)^{\frac{1}{2}}}{k_e}\right) \tag{20}$$

$$\begin{aligned} k_i^2 &= \frac{e^2}{k_B\epsilon_0}\frac{n_i}{T_i} \\ &= 2.099852429 \times 10^{-4} \text{ m K } \frac{n_i}{T_i} \end{aligned} \tag{21}$$

$$\begin{aligned} k_e^2 &= \frac{e^2}{k_B\epsilon_0}\frac{n_e}{T_e} \\ &= 2.099852429 \times 10^{-4} \text{ m K } \frac{n_e}{T_e} \end{aligned} \tag{22}$$

3 Data and Input Models

Calculation of absorption for a set of radio wave trajectories requires output ray paths from an ionospheric raytracer, as well as ionospheric parameters from a variety of models. Each of these are explained below.

3.1 Raytracer

The A-H absorption model described in this document utilizes output from a modified version of the Jones and Stephenson (1975) raytracer. The model calculates the index of refraction in a user-supplied model ionosphere using the Appleton-Hartree equations (assuming no collisions), and then numerically integrates the Hamiltonian ray path equations (Haselgrove, 1963) to yield a ray trajectory. When a ray intersects with the ground, it is assumed to undergo specular reflection off the ground. After a user specified number of bounces, or if the ray leaves the atmosphere, it ceases being calculated. By default, the raytracer only outputs information related to every time a ray bounces off the ground. This information includes the initial ray direction, the direction from which the ray reached the ground, and the path length. In order to utilize the A-H absorption model, the raytracer is also given optional arguments to output full ray trajectories.

The raytracer contains a simple, modular absorption framework that is able to combine absorption from multiple different absorption models for each ray path. However, this framework only accepts absorption models that report absorption in terms of vertical crossings of the D region at 30 MHz. For each ray landing, the approximate D region pierce point at 60 km is estimated by assuming a straight-line trajectory. Then, the absorption experienced by a radio wave passing through that point is calculated by summing contributions from the selected models. Contributions are adjusted to account for crossing the D region at oblique angles, and at frequencies other than 30 MHz if not accounted for by the model.

The raytracer uses a built-in, optional absorption model that estimates diurnal D region absorption with a method provided in Consultative Committee on International Radio (CCIR) report 252-2 (CCIR, 1970), which originally came from a US technical report (Lucas and Haydon, 1966). This model parameterizes absorption experienced by a radio wave of frequency f passing through the D region (in dB) as

$$L = \frac{667.2 \sec(\varphi)}{(f + f_B)^{1.98} + 10.2} I, \tag{23}$$

where φ is the radio wave angle of incidence with respect to the ionosphere. The parameter I represents the intensity of solar radiation, and is given by

$$I = (1 + 0.0037\, R_{12}) \cos^{1.3}(0.881\, X), \tag{24}$$

where R_{12} is the 12-month averaged sunspot number, and X is the solar zenith angle. All frequencies in the above equations are in MHz, and all spatially variable quantities are given at the D region pierce point (60 km altitude). Additional space weather-related sources of absorption are added using models such as D-RAP. In Section 5, diurnal D region absorption computed with the Lucas and Haydon (1966) absorption model is compared to absorption computed with the Appleton-Hartree absorption model for an example raytrace run.

3.2 E-CHAIM

The Empirical High Arctic Ionosphere Model (E-CHAIM) is an empirical model of E and F region electron density in the high latitude ($> 50°$) ionosphere (Themens et al., 2017; 2018; 2019). It is used as the source of electron density values for the A-H absorption model, and is the default model ionosphere used by the raytracer. E-CHAIM was chosen over other ionospheric models such as the International Reference Ionosphere (IRI, described in the following subsection) due to its generally superior accuracy at high latitudes (Themens et al., 2019). E-CHAIM represents ionospheric electron density with a series of spherical cap harmonic expansions of various ionospheric features determined from millions of ionosonde and radio occultation measurements. The large number of measurements incorporated into E-CHAIM allows it to reproduce diurnal, seasonal, and solar cycle variability in electron density.

E-CHAIM contains optional storm and precipitation submodels, which account for general ionospheric response to geomagnetic activity, and increased E-region ionization due to auroral precipitation respectively. While E-CHAIM only models the E and F regions by default, it also contains an optional D region submodel based on the Faraday International Reference Ionosphere 2018 (FIRI-2018) empirical model of the lower ionosphere (Friedrich et al., 2018). Due to the central role the D region plays in ionospheric absorption, it is highly recommended that the D region submodel is activated when computing absorption. FIRI-2018 parametrizes D region electron density based on altitude, solar zenith angle, latitude, and month of year. Notably, the FIRI-2018 (and consequently E-CHAIM) does not account for D region electron density perturbations due to auroral precipitation.

3.3 IRI

The International Reference Ionosphere (IRI) is a global, empirical model of the ionosphere (Bilitza et al., 2017) that incorporates ground and space measurements of the ionosphere to assemble monthly averages of ionospheric densities and temperatures between 50 and 2000 km altitude. Computation of the effective electron collision frequency used by the A-H absorption model requires information on the electron and ion temperature in the ionosphere. Since E-CHAIM only outputs electron densities, electron and ion temperatures are calculated using the IRI. Improved versions of the IRI model are released every

few years, and are named based on the year work on a given version was started. For implementation in the A-H model, the 2016 version of the IRI (IRI2016) was used.

3.4 NRLMSISE-00

The effective electron collision frequency requires neutral particle densities above the Earth, which are supplied by the US Naval Research Laboratory Mass Spectrometer and Incoherent Scatter Radar Exosphere (NRLMSISE-00) model. NRLMSISE-00 is an empirical model of neutral density in the atmosphere (Picone et al., 2002), incorporating incoherent scatter radar, mass spectrometer, and satellite drag measurements in order to supply neutral densities and temperatures from the ground to the exobase (~500-1000 km depending on solar activity). It is an extension of the Mass Spectrometer and Incoherent Scatter (MSIS-86) (Hedin, 1987) and Mass Spectrometer and Incoherent Scatter Exosphere (MSISE-90) (Hedin, 1991) models.

3.5 IGRF

The International Geomagnetic Reference Field (IGRF) is a model of the Earth's internal geomagnetic field (Alken et al., 2021), which is necessary to calculate the electron cyclotron frequency term in the Appleton-Hartree equation. The IGRF parameterizes the magnetic field with a set of spherical harmonic expansions, informed by many measurements of the Earth's magnetic field taken by a large variety of ground and space instruments.

4 Implementation

A procedure for calculating A-H absorption was formulated and implemented using output from the raytracing model. In the following description, a raytrace run can involve rays of multiple frequencies. This absorption model calculates the background absorption using the equations listed in Section 2 and the ionospheric models outlined in Section 3. The procedure is outlined in the following sections.

4.1 Set Up

Before the model is run, information needs to be pulled from the raytracer output and processed for use..

- For each frequency traced, a corresponding output file containing ray path trajectory information is loaded. Ray paths that escaped to space are discarded, and the remaining ray paths are filtered to include only those that landed within a set distance from some target (typically $50 - 100$ km). All remaining ray paths for each frequency are assembled into a single structure. Ray paths are initially in geographic coordinates (latitude, longitude, altitude).

- The density of points along a ray path is not constant along the path. To ensure there is a sufficient density of points when passing through the D region, all ray paths are interpolated to a set spatial resolution.

  - This interpolation is accomplished by converting each ray path to Cartesian, Earth-Centered Earth-Fixed (ECEF) coordinates, performing the interpolation, and converting back to geographic coordinates.

- While any spatial resolution could be used, 10 km is recommended to balance computation time and accuracy. For information on the impact of ray path spatial resolution on the results, see Appendix A.

- Latitude, longitude, and altitude ranges that contain all ray paths are determined. From these ranges, a 3D spatial grid is defined. This grid is referred to as the "base grid" going forward. The base grid uses step sizes of 0.4°, 0.4°, and 1 km for latitude, longitude, and altitude respectively by default. All models necessary for the absorption calculation are evaluated at the coordinates of the base grid.

4.2 Pre-Processing

The next step of the process is to call various empirical models in order to assemble spatial arrays of electron density, collision frequency, and magnetic field. All models should be called using input parameters such as date and time matching those supplied to the raytracer. These arrays are transformed into 3D interpolant functions. An interpolant function is a kind of data structure that can be called at arbitrary points, and returns values interpolated from the grid it is based on. In detail:

- Electron density is calculated using E-CHAIM for points on the base grid, and transformed into an interpolant for future use.

- A collision frequency array is calculated for points on the base grid, and an interpolant is created from that. This involves a number of steps:

  - The IRI2016 model is called to obtain electron and ion temperatures on the base grid. Due to the long computation time necessary for calling IRI2016 repeatedly, IRI2016 is called on a lower resolution grid (2° latitude, 2° longitude, 10 km altitude). This lower resolution grid is then interpolated to the base grid. Obtaining electron and ion temperatures from IRI2016 at a lower spatial resolution than other parameters was determined to have little to no effect on the resultant absorption based on internal testing.

  - The NRLMSISE-00 model is queried on the base grid to determine neutral densities for N_2, O_2, O, He, and H.

  - The electron and ion temperatures, neutral densities, and electron density are all used to compute electron-ion and electron-neutral collision frequencies on the base grid using Equations 9-14 and 19-22. These two collision frequencies are added together, and a collision frequency interpolant is created from the result.

- The IGRF model is queried for points on the base grid, and an interpolant is created. Note that the IGRF provides magnetic fields in the North-East-Down (NED) coordinate system, which varies with position on the Earth when compared to ECEF coordinates.
-

4.3 Absorption Computation

Now that the required interpolants have been created, absorption is integrated along each ray path as follows:

- The electron density, collision frequency, and magnetic field interpolants are each queried for every point along the ray path.

- Magnetic field values are rotated from NED coordinates to ECEF coordinates for comparison with the ray path.

- The ray path is converted from geographic to ECEF coordinates, and the propagation direction is computed for points along the ray path.

- Electron density, collision frequency, magnetic field, and propagation direction are all used to calculate the refractive index along the ray path using the Appleton-Hartree equations (Equations 2-7).

- Absorption is integrated along the ray path using the imaginary component of the refractive index according to Equation 1.

5 Example Run
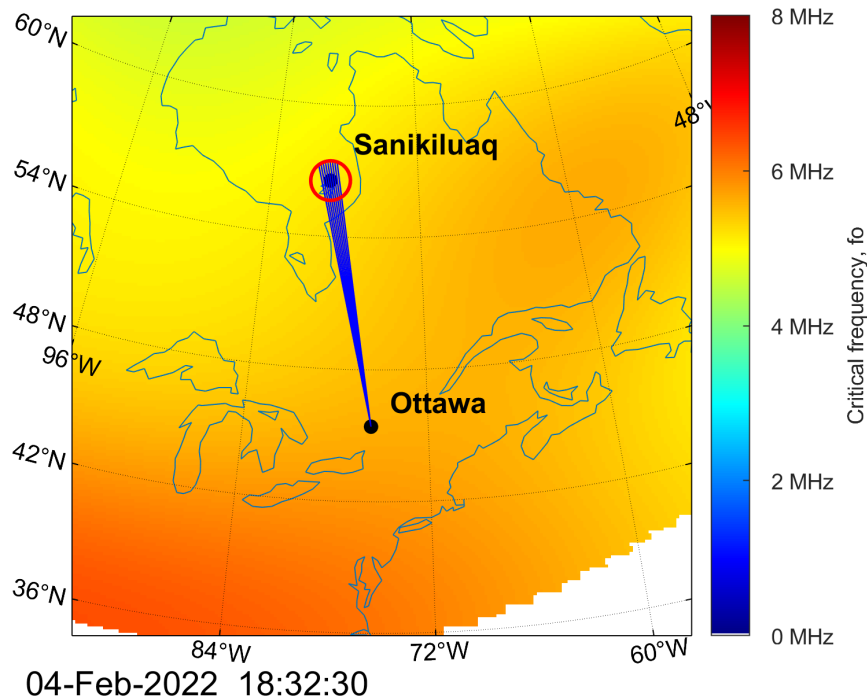
04-Feb-2022 18:32:30

Figure 1: Map showing critical frequency given by E-CHAIM for 4 February 2022 at 18:32:30 UTC, with 3.0 MHz raypaths starting at Ottawa that landed within 100 km of Sanikiluaq plotted in blue. Both Ottawa and Sanikiluaq are labelled, with the 100 km radius around Sanikiluaq indicated by a red circle. Map is in geographic coordinates.

In this section, the Appleton-Hartree absorption model is used to compute absorption for a typical set of raytraces. Ray paths were computed through an E-CHAIM ionosphere generated for 4 February 2022 at 18:32:30 UTC from Ottawa to Sanikiluaq. For this example run, ECHAIM's D region submodel was enabled, while the storm and precipitation submodels were disabled.

Rays were traced at elevation angles ranging from 1° to 89° in 0.2° increments, at azimuthal angles ranging from -2° to 2° from the great circle direction to Sanikiluaq in 0.5° increments, at frequencies from 3 to 18 MHz in 0.2 MHz increments. Rays that landed within 100 km of Sanikiluaq were considered to have reached the target and were selected for the absorption calculation. Figure 1 shows a map of critical frequency taken from the E-CHAIM electron density model, with the transmitter and target locations labelled. Critical frequency is proportional to the square root of the maximum electron density above a location, and indicates the maximum frequency of radio waves able to be reflected vertically by the ionosphere. The 3.0 MHz ray paths that landed within 100 km of the target are plotted in blue, along with a red 100 km circle around the target.

Absorption was calculated for all ray paths that reached Sanikiluaq assuming ordinary (O) mode propagation. As part of this process, various interpolants were assembled from different ionospheric models, as described in the previous section. Figure 2 shows vertical profiles of total (blue), electron-ion (orange) and electron-neutral (yellow) collision frequencies above Ottawa, constructed using the collision frequency interpolant. These profiles show clearly how electron-neutral collisions dominate in the lower ionosphere up to about 160 km, above which electron-ion collisions become dominant. It should be noted that in the interest of illustrating variation up to 450 km, the collision frequency interpolant was calculated up to 450 km altitude, even though ray paths only reached ~200 km maximum altitude.
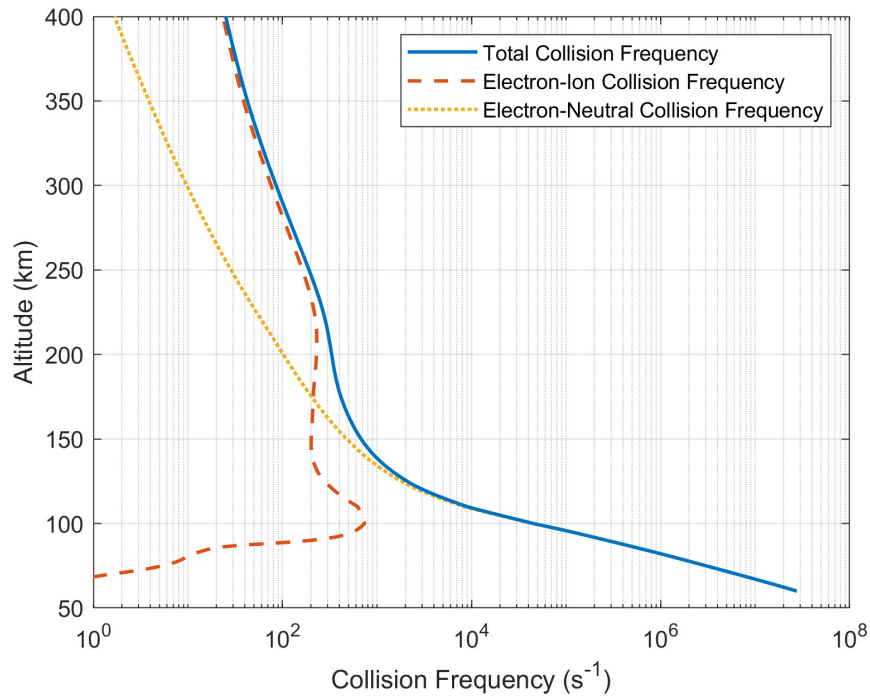
11

Figure 2: Height profiles of total (blue), electron-ion (orange), and electron-neutral (yellow) collision frequency, all output from interpolants used in calculating ionospheric absorption.

Figure 3 shows a single ray path from Ottawa to Sanikiluaq (top left), the absorption experienced by that ray versus latitude (bottom left), and the same absorption versus altitude (right). Points showing the original ray path output by the raytracer before being interpolated to a constant path length between points are plotted in the top left panel. The ray path considered here corresponds to a 6.4 MHz ray that was launched from Ottawa at 56° elevation, -11.42° azimuth, and underwent three hops before reaching Sanikiluaq. The altitude versus absorption seen in the right panel is multi-valued, due to the upward and downward path of the ray as it underwent multiple hops. The absorption per unit meter experienced by the ray seen in the bottom left and right panels varies significantly along the path. There are large peaks in absorption experienced by the ray as it passes through the D and E regions between 70 and 120 km. There are also smaller amounts of deviative absorption experienced by the ray as it reflects back to the Earth around 200 km, due to interaction with the F region.

Figure 4 shows a comparison between the A-H model absorption and the Lucas and Haydon (1966) absorption the raytracer uses by default for each ray that landed within 100 km of Sanikiluaq. Since ECHAIM's storm and precipitation models were not used for this example run, both the A-H model and the Lucas and Haydon (1966) absorption model only account for absorption resulting from D region diurnal solar ionization. While differences of up to 100 dB can be seen for some ray paths, absorption is higher in general for the Lucas and Haydon (1966) model than the A-H model, especially at the lowest frequencies. Since the Lucas and Haydon (1966) model is a semiempirical model based in part on measurements of absorption, it is possible some amount of space weather-related absorption is accounted for in the model. A-H absorption calculated using a similar example run in which ECHAIM's storm model was enabled was also compared to the Lucas and Haydon (1966) model (not shown), showing better agreement between the two models on average, albeit with a similar amount of scatter.
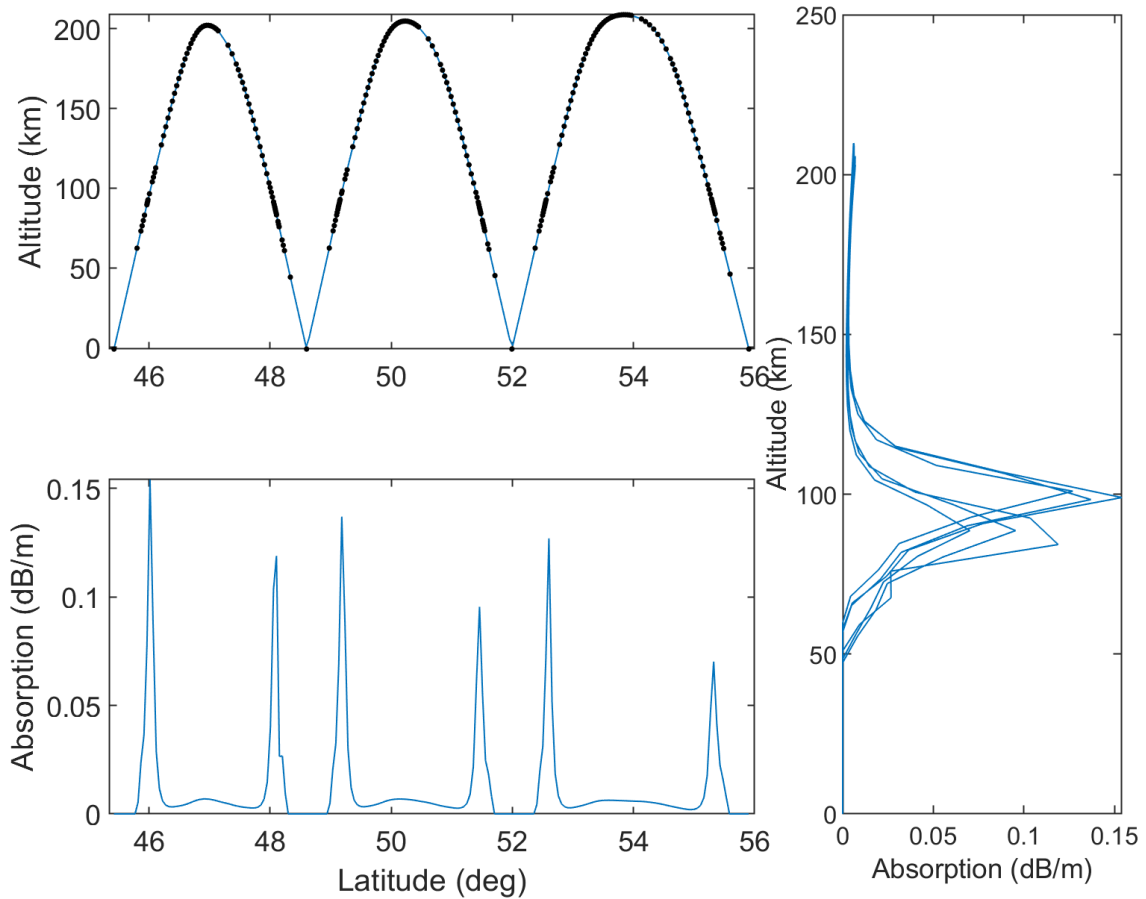
Figure 3: (top left) Altitude versus Latitude for a single 6.4 MHz ray launched from Ottawa at 55.4° elevation and -10.92° azimuth, that underwent three hops before reaching Sanikiluaq. Black points show the original points making up the raypath, before being interpolated to a constant path length between points. (bottom left) Absorption (in dB/m) experienced by the same ray as above versus latitude, output from the A-H absorption model assuming O mode propagation. (right) Absorption experienced by the ray vs altitude.

Absorption experienced by a radio wave reduces the signal power received at some target. Figure 5 shows signal power versus frequency and initial elevation angle for this example run using three different absorption methods. In the top panel, absorption was calculated using the raytracer's built in Lucas and Haydon (1966) diurnal D region absorption model based on D region crossings. In the bottom left panel, absorption was calculated using the A-H model assuming O mode propagation while in the bottom right panel extraordinary (X) mode propagation was assumed.. Ray paths used for the absorption calculation in the lower right panel were traced with X mode propagation, in contrast to the other two panels, which were traced with O mode propagation.

While received signal power at frequencies > 8 MHz is approximately the same for all three absorption methods, there are significant differences at lower frequencies. At lower frequencies, compared to the D region crossing method, the A-H method (both X and O mode) results in less absorption and more signal power for lower elevation rays, and more absorption (less signal power) for higher elevation rays. Comparing the O and X modes for the A-H method, the X mode results in increased absorption at lower frequencies in general. All bands of signal power in the X mode panel reach slightly higher frequencies than the other two panels. This effect is a consequence of the slightly different paths taken by X mode versus O mode rays, and is not related to the absorption model. Absorption varies significantly depending on ionospheric conditions, and the details of the propagation path, so these trends may not apply in general.
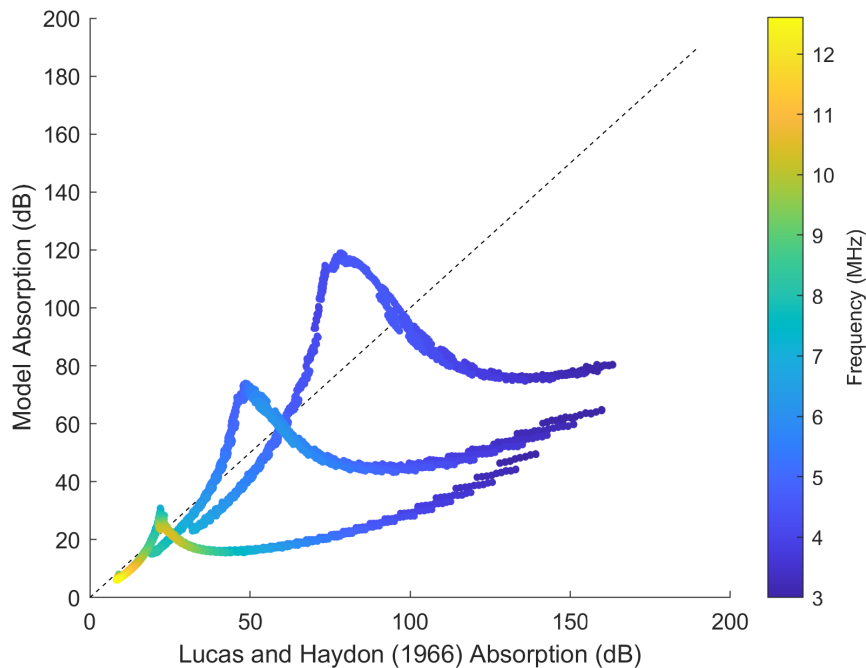
Figure 4: Model absorption versus Lucas and Haydon (1966) absorption for each ray that landed within 100 km of Sanikiluaq. Ray frequencies are indicated by color.

6 Caveats and Considerations

When using the A-H absorption model outlined in this document, some points and caveats should be considered.

Most importantly, only sources of absorption that are accounted for in the constituent ionospheric models used by the absorption model will contribute to total absorption. For example, auroral absorption is a type of absorption resulting from increased D and E region ionization in the auroral zone during times of increased geomagnetic activity. E-CHAIM's 'precipitation' submodel adds additional electron density to the E region ionosphere related to auroral precipitation. However, the D region submodel (FIRI-2018) does not account for auroral precipitation. Therefore, the A-H absorption model can only account for auroral absorption that occurs in the E region. In contrast, the increased ionospheric electron density associated with solar flares known to cause shortwave fadeout is not accounted for at all in E-CHAIM, and so the subsequent calculated absorption cannot include the effects of shortwave fadeout. Of the major sources of space weather-related ionospheric absorption, the A-H model can partially account for auroral absorption, and cannot account for shortwave fadeout or polar cap absorption.

Absorption associated with shortwave fadeout and polar cap absorption is often estimated with empirical models such as D-RAP or the Optimised D-Region Absorption Model (ODRAM) (Rogers and Honary, 2020). It is possible to combine the A-H model absorption detailed here with these empirical absorption models. However, care should be taken to ensure sources of absorption are not counted twice. For example, ODRAM estimates absorption resulting from shortwave fadeout, polar cap absorption and auroral absorption. However, since E-CHAIM already partially accounts for increased electron density associated with auroral activity, adding ODRAM derived absorption on top of the A-H model absorption would result in auroral absorption being added twice.
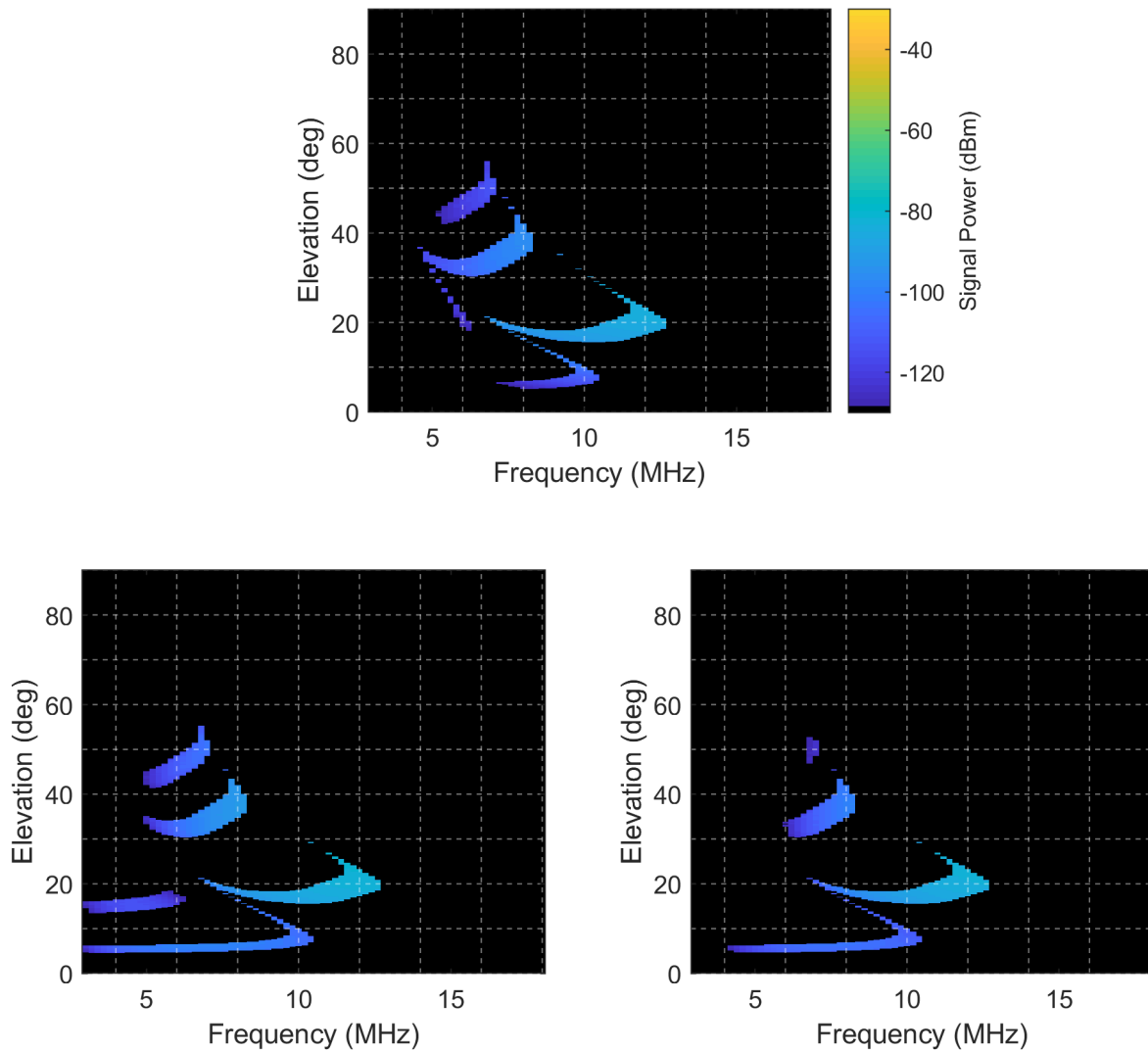
Figure 5: Raytraced signal power versus frequency and elevation detected by a theoretical receiver in Sanikiluaq using the following absorption models: (top) Lucas and Haydon (1966) diurnal D-region absorption, (bottom left) A-H Model assuming O mode propagation, (bottom right) A-H model using X mode propagation. All raytraces were performed through a model ionosphere generated by E-CHAIM for 4 February 2022 at 18:32:30 UTC. Ray frequencies are indicated by color.

Another factor to consider is the diversity of models used as input for the absorption model. Since input parameters such as electron density, electron and ion temperatures, and neutral densities come from different, independent models, the spatial variation of these different parameters do not necessarily line up physically. For example, auroral precipitation is known to cause heating in the ionosphere (e.g. Banks, 1977) along with the increased electron density. While E-CHAIM correctly adds the increased electron density associated with auroral precipitation, it does not provide temperature information. Instead, temperature data is pulled from the IRI, which does not account for auroral precipitation. Therefore, electron density and temperature data used by the absorption model are not consistent. This is a consequence of using different, distinct ionospheric models for different parameters. Sourcing all ionospheric parameters from the same ionospheric model would be preferable. However, such a model does not exist at this time.

7 Summary

This report has described the implementation and integration of a piecewise absorption model into an existing ionospheric HF radio raytracing program. This absorption model utilizes distinct ionospheric models of various ionospheric parameters to estimate the absorption experienced by a radio wave that has travelled a specific propagation path output by the raytracer. The theory, formulas, and ionospheric models driving the absorption model were described in detail. Specifics of how absorption is calculated using these models and formula were described, and a trial run was presented and analyzed in detail.

For the trial run, absorption results obtained using the absorption model were compared to the Lucas and Haydon (1966) diurnal D region absorption model. While absorption values obtained with the two methods were similar on average, absorption calculated for individual ray paths were markedly different. When distinguishing propagation paths by initial ray elevation, the new absorption model described here resulted in lower absorption for lower initial elevation rays, and higher absorption for higher initial elevation rays.

Some considerations to pay attention to when using the model were noted. Most importantly, the Appleton-Hartree absorption model can only output absorption from sources that are accounted for in its constituent ionospheric models. This means that auroral absorption can be partially accounted for, and both shortwave fadeout and polar cap absorption cannot. Additionally, care should be taken when combining this model with other models of absorption for specific space weather phenomena that certain absorption sources are not counted twice. Finally, it was also noted that since different ionospheric parameters have been sourced from different ionospheric models, these parameters are not necessarily consistent with each other.

8 References

Aggarwal, K.M., Nath, N., Setty, C.S.G.K., 1979. Collision frequency and transport properties of electrons in the ionosphere. Planetary and Space Science 27, 753–768. https://doi.org/10.1016/0032-0633(79)90004-7

Alken, P., Thébault, E., Beggan, C.D., Amit, H., Aubert, J., Baerenzung, J., Bondar, T.N., Brown, W.J., Califf, S., Chambodut, A., Chulliat, A., Cox, G.A., Finlay, C.C., Fournier, A., Gillet, N., Grayver, A., Hammer, M.D., Holschneider, M., Huder, L., Hulot, G., Jager, T., Kloss, C., Korte, M., Kuang, W., Kuvshinov, A., Langlais, B., Léger, J.-M., Lesur, V., Livermore, P.W., Lowes, F.J., Macmillan, S., Magnes, W., Mandea, M., Marsal, S., Matzka, J., Metman, M.C., Minami, T., Morschhauser, A., Mound, J.E., Nair, M., Nakano, S., Olsen, N., Pavón-Carrasco, F.J., Petrov, V.G., Ropp, G., Rother, M., Sabaka, T.J., Sanchez, S., Saturnino, D., Schnepf, N.R., Shen, X., Stolle, C., Tangborn, A., Tøffner-Clausen, L., Toh, H., Torta, J.M., Varner, J., Vervelidou, F., Vigneron, P., Wardinski, I., Wicht, J., Woods, A., Yang, Y., Zeren, Z., Zhou, B., 2021. International Geomagnetic Reference Field: the thirteenth generation. Earth Planets Space 73, 49. https://doi.org/10.1186/s40623-020-01288-x

Banks, P.M., 1977. Observations of joule and particle heating in the auroral zone. Journal of Atmospheric and Terrestrial Physics 39, 179–193. https://doi.org/10.1016/0021-9169(77)90112-X

Bilitza, D., Altadill, D., Truhlik, V., Shubin, V., Galkin, I., Reinisch, B., Huang, X., 2017. International Reference Ionosphere 2016: From ionospheric climate to real-time weather predictions. Space Weather 15, 418–429. https://doi.org/10.1002/2016SW001593

Davies, K., 1990. Ionospheric Radio, Ionospheric Radio. Peter Peregrinus Ltd. https://doi.org/10.1049/pbew031e

Fiori, R.A.D., Chakraborty, S., Nikitina, L., 2022. Data-based optimization of a simple shortwave fadeout absorption model. Journal of Atmospheric and Solar-Terrestrial Physics 230, 105843. https://doi.org/10.1016/j.jastp.2022.105843

Friedrich, M., Pock, C., Torkar, K., 2018. FIRI-2018, an Updated Empirical Model of the Lower Ionosphere. Journal of Geophysical Research: Space Physics 123, 6737–6751. https://doi.org/10.1029/2018JA025437

George, P.L., Bradley, P.A., 1974. A new method of predicting the ionospheric absorption of high frequency waves at oblique incidence. ITU Telecommunication Journal 41, 307–312.

Haselgrove, J., 1963. The Hamiltonian ray path equations. Journal of Atmospheric and Terrestrial Physics 25, 397–399. https://doi.org/10.1016/0021-9169(63)90173-9

Hedin, A.E., 1991. Extension of the MSIS Thermosphere Model into the middle and lower atmosphere. Journal of Geophysical Research: Space Physics 96, 1159–1172. https://doi.org/10.1029/90JA02125

Hedin, A.E., 1987. MSIS-86 Thermospheric Model. Journal of Geophysical Research: Space Physics 92, 4649–4662. https://doi.org/10.1029/JA092iA05p04649

Jones, R.M., Stephenson, J.J., 1975. A versatile three-dimensional ray tracing computer program for radio waves in the ionosphere. OT Report 75-76 185.

Lucas, D.L., Haydon, G.W., 1966. Predicting Statistical Performance Indexes for High Frequency Ionospheric Telecommunications Systems.

Mitra, A.P., 1974. Ionospheric effects of solar flares. https://doi.org/10.1007/978-94-010-2231-6

National Research Council, 2008. Severe Space Weather Events: Understanding Societal and Economic Impacts: A Workshop Report. Washington, DC: The National Academies Press. https://doi.org/10.17226/12507

Pederick, L.H., Cervera, M.A., 2014. Semiempirical Model for Ionospheric Absorption based on the NRLMSISE-00 atmospheric model: PEDERICK AND CERVERA. Radio Sci. 49, 81–93. https://doi.org/10.1002/2013RS005274

Picone, J.M., Hedin, A.E., Drob, D.P., Aikin, A.C., 2002. NRLMSISE-00 empirical model of the atmosphere: Statistical comparisons and scientific issues. Journal of Geophysical Research: Space Physics 107, SIA 15-1-SIA 15-16. https://doi.org/10.1029/2002JA009430

Riddolls, R., 2006. A Canadian perspective on high-frequency over-the-horizon radar. (DRDC Ottawa TM 2006-285). Defence R&D Canada – Ottawa.

Rogers, N.C., Honary, F., 2020. ODRAM: Optimised D-region Absorption Model, Software User Guide, Software Version 1.6.

Sauer, H.H., Wilkinson, D.C., 2008. Global mapping of ionospheric HF/VHF radio wave absorption due to solar energetic protons. Space Weather 6. https://doi.org/10.1029/2008SW000399

Schumer, E.A., 2010. Improved Modeling of Midlatitude D-region Ionospheric Absorption of High Frequency Radio Signals during Solar X-ray Flares.

Schunk, R., Nagy, A., 2009. Ionospheres: Physics, Plasma Physics, and Chemistry, 2nd ed, Cambridge Atmospheric and Space Science Series. Cambridge University Press, Cambridge. https://doi.org/10.1017/CBO9780511635342

Schunk, R.W., Nagy, A.F., 1978. Electron temperatures in the F region of the ionosphere: Theory and observations. Rev. Geophys. 16, 355. https://doi.org/10.1029/RG016i003p00355

Thayaparan, T., Dupont, D., Ibrahim, Y., Riddolls, R., 2019. High-frequency ionospheric monitoring system for over-the-horizon radar in Canada. IEEE Transactions on Geoscience and Remote Sensing 57, 6372–6384. https://doi.org/10.1109/TGRS.2019.2905757

Thayaparan, T., Ibrahim, Y., Polak, J., Riddolls, R., 2018. High-Frequency Over-the-Horizon Radar in Canada. IEEE Geoscience and Remote Sensing Letters 15, 1700–1704. https://doi.org/10.1109/LGRS.2018.2856185

Thayaparan, T., Marchioni, J., Kelsall, A., Riddolls, R., 2020. Improved Frequency Monitoring System for Sky-Wave Over-the-Horizon Radar in Canada. IEEE Geoscience and Remote Sensing Letters 17, 606–610. https://doi.org/10.1109/LGRS.2019.2928172

Themens, D.R., Jayachandran, P.T., Bilitza, D., Erickson, P.J., Häggström, I., Lyashenko, M.V., Reid, B., Varney, R.H., Pustovalova, L., 2018. Topside Electron Density Representations for Middle and High Latitudes: A Topside Parameterization for E-CHAIM Based On the NeQuick. Journal of Geophysical Research: Space Physics 123, 1603–1617. https://doi.org/10.1002/2017JA024817

Themens, D.R., Jayachandran, P.T., Galkin, I., Hall, C., 2017. The Empirical Canadian High Arctic Ionospheric Model (E-CHAIM): NmF2 and hmF2. Journal of Geophysical Research: Space Physics 122, 9015–9031. https://doi.org/10.1002/2017JA024398

Themens, D.R., Jayachandran, P.T., McCaffrey, A.M., Reid, B., Varney, R.H., 2019. A Bottomside Parameterization for the Empirical Canadian High Arctic Ionospheric Model. Radio Science 54, 397–414. https://doi.org/10.1029/2018RS006748

Warrington, E.M., Stocker, A.J., Siddle, D.R., Hallam, J., Al-Behadili, H.A.H., Zaalov, N.Y., Honary, F., Rogers, N.C., Boteler, D.H., Danskin, D.W., 2016. Near real-time input to a propagation model for nowcasting of HF communications with aircraft on polar routes. Radio Science 51, 1048–1059. https://doi.org/10.1002/2015RS005880

Zawdie, K.A., Drob, D.P., Siskind, D.E., Coker, C., 2017. Calculating the absorption of HF radio waves in the ionosphere. Radio Science 52, 767–783. https://doi.org/10.1002/2017RS006256

Appendix A: Evaluating Ray Path Spatial Resolution

Ray paths output by the raytracer are comprised of irregularly spaced points. Generally, there are more points where the ray path passes through regions of high electron density, and less in places where it passes through regions of lower electron density. This is not ideal for computation of absorption, since a significant amount of absorption happens in the D region; a region with relatively low electron density and high neutral density. To ensure the ray path samples a sufficient number of points in all ionospheric regions, ray paths are interpolated to a constant spatial resolution. Selection of this spatial resolution has to balance accuracy and runtime. Since all ionosphere models are called with a spatial resolution of 0.4° latitude and longitude (~50 km in latitude, ~30 km in longitude at 60° latitude) , and 1 km in altitude, presumably any spatial resolution less than 1 km would capture all variation in the ionospheric model outputs.

To decide on a default spatial resolution, absorption was calculated with the A-H model on the same set of raytrace runs presented in Section 5 using 0.1, 1, 10, and 20 km spatial resolutions on a Lenovo Thinkpad T480 laptop computer. A 0.1 km resolution was used as a baseline to which the other three spatial resolutions were compared, since it is an order of magnitude smaller than the smallest model resolution. Table 1 shows the computation time for an absorption calculation for all four resolutions, as well as mean error and percent error for 1, 10, and 20 km when compared to 0.1 km.

First examining computation time, the 0.1 km spatial resolution calculation took much longer than the other three resolutions to compute. This is likely a result of the high-resolution ray paths being too large

Spatial Resolution (km)	Computation Time (s)	Mean error (dB) (compared to 0.1 km)	Mean Percent Error (compared to 0.1 km)
0.1	~15000	-	-
1	102.4	0.039	0.057
10	76.8	0.51	0.79
20	61.1	1.5	2.9

Table 1: Computation time, mean error, and mean percent error for absorption calculations using different raypath spatial resolutions. Error values are established by comparison with 0.1 km results. All raytraces were performed through a model ionosphere generated by E-CHAIM for 4 February 2022 at 18:32:30 UTC.

to fit in RAM, leading to a significant slowdown as the system moved data back and forth between the RAM and hard drive. The other three resolutions took a much more reasonable amount of time to run. Using a 10 km resolution took ~25% longer than 20 km, and 1 km took ~34% longer than 10 km. All three resolutions resulted in a fairly small error when compared to 0.1 km. The largest error seen was on average 1.5 dB (or ~3%) for 20 km compared to 0.1 km. Both 10 and 1 km resolutions resulted in < 1% mean percent errors compared to 0.1 km.

Figure 6 shows histograms of absorption error when compared to 0.1 km for 1, 10, and 20 km for all rays that reached Sanikiluaq. The distribution in all three cases peak at 0 dB, with most absorption errors clustering around zero. Generally, errors for 20 km are less than 10 dB, errors for 10 km are less than 4 dB, and errors for 1 km are less than 0.2 dB. There is a small population of errors between 0.2 and 0.4 dB for 1 km resolution. This population is probably the result of a small ionospheric feature that was not sufficiently sampled at 1 km resolution. Based on the these results, a default ray path spatial resolution of 10 km was chosen as a good balance between computation time and error, especially for situations where time is limited. However, since the spatial resolution is user selectable, it is suggested that 1 km resolution be used if time is not a factor.
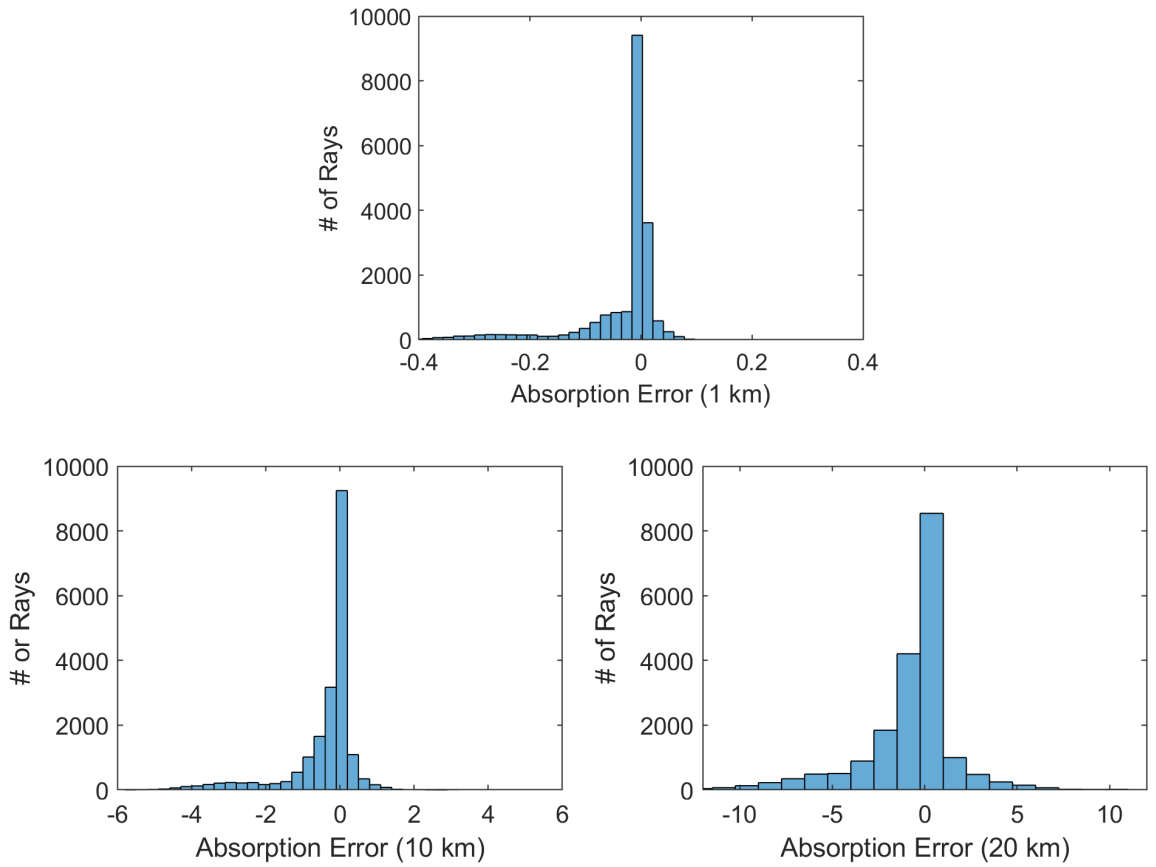
Figure 6: Histograms of absorption error (when compared to 0.1 km resolution) for (top) 1 km, (bottom left) 10 km, and (bottom right) 20 km raypath spatial resolution for rays that landed within 100 km of Sanikiluaq. All raytraces were performed through a model ionosphere generated by E-CHAIM for 4 February 2022 at 18:32:30 UTC.